

# Joint Unsupervised Learning for the Vertebra Segmentation, Artifact Reduction and Modality Translation of CBCT Images

Yuanyuan Lyu  
Z2SKY

Haofu Liao  
University of Rochester

Heqin Zhu  
USTC

S. Kevin Zhou  
ICT

## Abstract

We investigate the unsupervised learning of the vertebra segmentation, artifact reduction and modality translation of CBCT images. To this end, we formulate this problem under a unified framework that jointly addresses these three tasks and intensively leverages the knowledge sharing. The unsupervised learning of this framework is enabled by 1) a novel shape-aware artifact disentanglement network that supports different forms of image synthesis and vertebra segmentation and 2) a deliberate fusion of knowledge from an independent CT dataset. Specifically, the proposed framework takes a random pair of CBCT and CT images as the input, and manipulates the synthesis and segmentation via different combinations of the decodings of the disentangled latent codes. Then, by discovering various forms of consistencies between the synthesized images and segmented, the learning is achieved via self-learning from the given CBCT and CT images obviating the need for the paired (i.e., anatomically identical) groundtruth data. Extensive experiments on clinical CBCT and CT datasets show that the proposed approach performs significantly better than other state-of-the-art unsupervised methods trained independently for each task and, remarkably, the proposed approach achieves a dice coefficient of 0.879 for unsupervised CBCT vertebra segmentation.

## 1. Introduction

Cone-beam computed tomography (CBCT) has been widely used in spinal surgery as an intraoperative 3D imaging modality to guide the intervention. However, compared with the conventional computed tomography (CT), intraoperative CBCT images have more pronounced noise and poor tissue contrast [20, 21]. Moreover, it is also common to have metallic objects presented during the imaging, which introduces metal artifacts and further degrades the quality of CBCT images [28, 18]. On the other hand, identifying the vertebrae is of great importance to the spinal surgery. The poor CBCT image quality makes it challenging to delineate the vertebra shape and, thus, compromises the intervention.

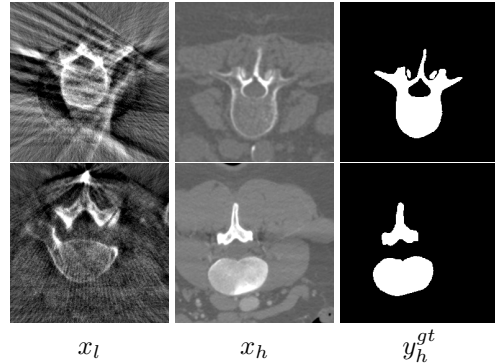


Figure 1. Sample images  $x_l$  from the CBCT domain,  $x_h$  from the CT domain and the corresponding vertebra ground truth  $y_h^{gt}$  of  $x_h$ . Due to the lack of groundtruth high-quality CBCT image and vertebra annotations, learning to improve the CBCT image quality and segment the CBCT vertebrae is challenging. We propose to leverage the knowledge from CT (both image and shape) to address this challenge.

To address the problem, this study aims to design a computational method to improve the quality of the CBCT images and facilitate the delineation of vertebrae. At the same time, this study also aims to design a vertebra segmentation method to automate the delineation and leverages this task to, in turn, improve the CBCT image quality. For either task, we find it clinically impractical to train the model in a supervised manner. First, it is difficult to find a pair of anatomically identical CBCT images, one is low quality and the other is high quality. A common practice [27, 25] is to synthesize artifacts in high-quality images to create the anatomically paired data. However, models trained with synthesized data usually generalize poorly to clinical images. Second, it is also challenging to manually annotate the CBCT images due to the low quality. As shown in Fig. 1, the vertebrae in CBCT images may be corrupted and the annotation requires a great deal of expertise and label work.

Therefore, this study resorts to develop an unsupervised method to improve the image quality and segment the vertebrae of CBCT images. To enable the unsupervised learning, we notice that it might be possible to learn from an independent CT image dataset. On the one hand, CT images

are generally with high quality (e.g., less pronounced artifacts, high contrast, and high signal-to-noise ratio) and the anatomical details can be well observed. On the other hand, annotating the CT images is relatively cheaper and there are several public spinal CT datasets with segmentation labels available <sup>1</sup>. For the former, we may design a model that learns from the CT image domain about how high-quality images should look like and apply the knowledge to improve the quality of CBCT images. For the latter, we may design a model that learns from the vertebra segmentation of CT images and apply the knowledge to segment CBCT vertebrae. Learning these two models together essentially defines an unsupervised vertebra segmentation, artifact reduction, and modality transfer problem.

Instead of developing models to independently address each task, we formulate this problem under a unified framework that jointly addresses these three tasks and intensively leverages the knowledge sharing. In particular, we propose a novel shape-aware artifact disentanglement network that 1) supports different forms of image synthesis and vertebra segmentation, 2) shares the knowledge learned from different synthesis and segmentation tasks, and 3) discovers different forms of consistencies between the inputs and outputs. Specifically, given a random pair of CBCT and CT images, the proposed framework encodes disentangled representations and manipulates the synthesis and segmentation via different combinations of the decodings. The encoders, decoders and segmentors are reapplied during the synthesis and segmentation to share the knowledge. Then, by discovering various forms of consistencies between the synthesized images and segmented vertebrae, self-learning from the given CBCT and CT images is achieved, and no paired data for the CBCT is necessary.

In summary, the contributions of this work are threefold:

- By utilizing disentangled representations and anatomical knowledge from the target domain, we introduce a *unified framework for unsupervised vertebra segmentation, artifact reduction, and modality translation*. These tasks benefit from each other through the joint unsupervised learning.
- We propose a *novel shape-aware artifact disentanglement network* that supports different forms of image synthesis and vertebra segmentation and discovers different forms of consistencies between the inputs and outputs to enable the unsupervised learning.
- We propose to use a *shape-aware normalization layer* to explicitly fuse the anatomical information, learned through shape consistency, into the decoder and boost the image synthesis performance.

---

<sup>1</sup><http://spineweb.digitalimaginggroup.ca/>

## 2. Related Works

Our approach is related to multiple lines of research. Below we briefly introduce related literature of unpaired image-to-image translation, the use of normalization in style transfer, and unsupervised segmentation.

### 2.1. Unpaired Image-to-Image Translation

Isola *et al.* [10] introduce a simple framework with conditional GANs as structural loss for image-to-image translation with paired data. CycleGAN [30] and UNIT [14] extend the work to unpaired images with a cycle-consistent mechanism. MUNIT [8] and DRIT [12] further embed different images into a common content space and manipulate the domain-specific attributes to generate diverse images. Recently, Liao *et al.* [13] propose a novel artifact disentanglement network (ADN) with specialized encoders and decoders handling metal artifacts and achieve great MAR performance on clinical data including CBCT images. However, image synthesis without explicit anatomy constrain may lead to inconsistent anatomical structure which is dangerous in medical area. Zhang *et al.* [29] use the anatomical information of both domains to ensure structural invariance in modality translation. Their framework can not be applied in our circumstance because only segmentations from CT domain is available.

### 2.2. Normalization in Style Transfer

Ioffe *et al.* [9] first introduce batch normalization (BN), which eases the training of DNNs. While in style transfer, replacing BN by instance normalization (IN) could significantly improve the image generation performance [23] and IN is suggested to perform some kind of style normalization [7]. Later on, conditional normalization layers are designed [3, 7, 16]. The new layers first normalized activations to zero mean and unit deviation and then denormalize them with learned affine transformation from external data. In this way, conditional BN [3] and Adaptive IN (AdaIN) [7] control the style globally and SPatially Adaptive DENormalization (SPADE) [16] modulates the activations spatially. SPADE shows advantages over other normalization layers in image synthesis. As the semantic mask used to learn spatial transformation is not available here, we propose to adapt SPADE with shape information extracted from disentangled feature representation.

### 2.3. Unsupervised Segmentation

Annotations for medical images are time consuming with trained experts and such data often come from different domains (i.e. different modalities, protocols, sites). A model trained on source domain hardly works well on target domain. To solve the problem, recently works learn domain-invariant features and anatomical prior by adversar-

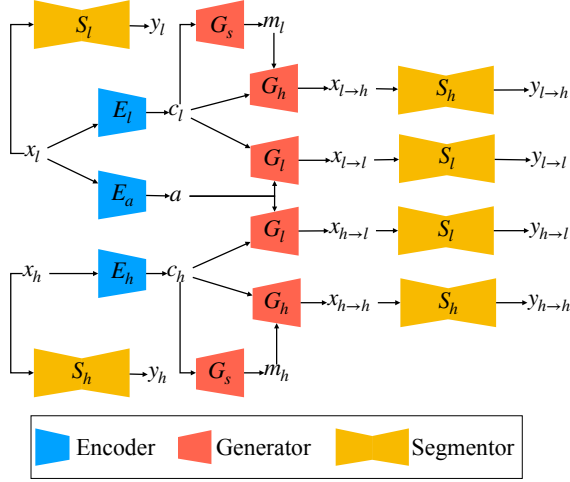


Figure 2. Architecture of the proposed shape-aware artifact disentangled network.

ial networks [11, 2] or apply segmentation after image translation as an ad-hoc approach [24]. However, when domain adaption or synthesis fails, the segmentation algorithm can not output correct results.

### 3. Methodology

Let  $X_l$  be the domain of low-quality CBCT images,  $X_h$  be the domain of high-quality CT images, and  $Y$  be the domain of vertebra shapes. A CBCT image  $x_l \in X_l$  is usually noisy and may contain streak artifacts while a CT image  $x_h \in X_h$  are artifact-free and provide more anatomical details. A vertebra shape  $y \in Y$  can be presented as a binary segmentation mask where  $y(k) \in \{0, 1\}$  indicates whether a pixel at location  $k$  belongs to a vertebra. Figure 1 shows samples from these three domains.

The proposed approach aims to improve the quality of images in  $X_l$  as well as learn their vertebra shapes  $Y$  under an unsupervised scenario. That is, given a set of low-quality images  $\mathcal{D}_l = \{x_l \mid x_l \in X_l\}$ , we aim to learn a translator  $\mathcal{F} : X_l \rightarrow X_h \times Y$  that maps  $x_l$  to its corresponding high-quality image  $x_h \in X_h$  and vertebra shape  $y_l \in Y$  without having paired (i.e., anatomically identical) groundtruth data  $x_h$  and  $y_l^{gt}$  available for supervision. To facilitate this unsupervised learning, we also assume the availability of a high-quality image dataset  $\mathcal{D}_h = \{(x_h, y_h^{gt}) \mid x_h \in X_h, y_h^{gt} \in Y, y_h^{gt} = \mathcal{S}_h(x_h)\}$  where  $\mathcal{S}_h : X_h \rightarrow Y$  is a segmentor that maps a high-quality CT image  $x_h$  to its corresponding vertebra shape  $y_h^{gt}$ . Note that  $\mathcal{D}_l$  and  $\mathcal{D}_h$  are independent, i.e., they are collected from different patients. Next, we introduce how to leverage the knowledge from this independent dataset  $\mathcal{D}_h$  for the unsupervised learning of  $\mathcal{F}$  from  $\mathcal{D}_l$ .

Given two independent datasets  $\mathcal{D}_l$  and  $\mathcal{D}_h$ , learning the translation between  $X_l$  and  $X_h$  is essentially an unsuper-

vised cross-modality artifact reduction problem. Similar to the idea by Liao *et al.* [13], we propose to address this task via artifact disentanglement. As this work also aims to learn vertebra shapes of  $X_l$ , we propose a shape-aware artifact disentanglement approach that takes the vertebra shape learning into consideration, and jointly improves artifact reduction and vertebra segmentation.

In artifact disentanglement, we assume that the content (i.e., bones, soft tissues, etc.) and the artifacts (i.e., noises, streaks, etc.) of low-quality images  $X_l$  can be encoded separately in the latent space. For high-quality images  $X_h$ , there are no artifacts and therefore only the content will be encoded. This disentanglement allows decodings between the different combinations of the artifact and content components of  $X_l$  and  $X_h$ , which enables different forms of generations (Section 3.1). The unsupervised learning is achieved by designing losses that encourage the generations enabled by artifact disentanglement (Section 3.2).

More importantly, we fuse the shape representation learning into the artifact disentanglement. On the one hand, we leverage the learned vertebra shapes as attentions to guide the generations for better artifact reduction (Section 3.1). On the other hand, we leverage the generated images to discover the consistency in vertebra shapes and achieve unsupervised vertebra segmentation (Section 3.2).

#### 3.1. Network Architecture

An overview of the network architecture of the proposed approach is shown in Figure 2. Our network takes two unpaired images  $x_l \in X_l$  and  $x_h \in X_h$  as inputs. For  $x_l$ , we use a content encoder  $E_l$  and an artifact encoder  $E_a$  to encode its content and artifact components, respectively. As  $x_h$  does not contain artifacts, we only use a content encoder  $E_h$  to encode its content. The latent codes are written as:

$$c_l = E_l(x_l), c_h = E_h(x_h), a = E_a(x_l). \quad (1)$$

With four different combinations of the decodings, our network has four outputs  $x_{l \rightarrow l}$ ,  $x_{l \rightarrow h}$ ,  $x_{h \rightarrow l}$ , and  $x_{h \rightarrow h}$ , where  $x_{i \rightarrow j}$  means the output is encoded with the content of  $x_i$ ,  $i \in \{l, h\}$  and intended to look like a sample from  $X_j$ ,  $j \in \{l, h\}$ . We use two different decoders  $G_l$  and  $G_h$  to generate the four outputs. The low-quality image decoder  $G_l$  takes a content code  $c_i$ ,  $i \in \{l, h\}$  and an artifact code  $a$  as inputs and outputs a low-quality image  $x_{i \rightarrow l}$ :

$$x_{l \rightarrow l} = G_l(c_l, a), x_{h \rightarrow l} = G_l(c_h, a). \quad (2)$$

Note that  $x_{l \rightarrow l}$  is encoded and decoded entirely from  $x_l$  and thus should look identical to  $x_l$ .  $x_{h \rightarrow l}$  is encoded with the content of  $x_h$  and the artifact of  $x_l$ , and thus should match the content of  $x_h$  but contain artifacts transferred from  $x_l$ .

The high-quality image decoder  $G_h$  takes a content code  $c_i$ ,  $i \in \{l, h\}$  and a vertebra shape attention map  $m_i$  as in-

puts and outputs a high-quality image  $x_{i \rightarrow h}$ :

$$x_{l \rightarrow h} = G_h(c_l, m_l), x_{h \rightarrow h} = G_h(c_h, m_h), \quad (3)$$

where the shape attention map  $m_i = G_s(c_i)$  is generated by a shape decoder  $G_s$ . We use  $m_i$  to explicitly fuse the vertebra shape information into the decoding such that  $G_h$  generates better the vertebra region which is critical in clinical practice. We will also show later (Section 3.2) that learning  $m_i$  can be achieved using the vertebra shapes  $y_h^{gt}$  from  $G_h$ . Also, note that  $x_{h \rightarrow h}$  is generated from the content of  $x_h$  and thus should be identical to  $x_h$ .  $x_{l \rightarrow h}$  is generated only using the content of  $x_l$  and thus anatomically look like  $x_l$  but with the artifacts removed and quality improved, which is exactly what we aim to achieve in this work.

Another goal of this work is to segment vertebra shapes  $Y$  from  $X_l$ . To this end, we use a low-quality image segmentor  $S_l$  to map images from domain  $X_l$  to space  $Y$ :

$$y_l = S_l(x_l), y_{l \rightarrow l} = S_l(x_{l \rightarrow l}), y_{h \rightarrow l} = S_l(x_{h \rightarrow l}). \quad (4)$$

Likewise, we also use a high-quality image segmentor  $S_h$  to map images from domain  $X_h$  to space  $Y$ :

$$y_h = S_h(x_h), y_{h \rightarrow h} = S_h(x_{h \rightarrow h}), y_{l \rightarrow h} = S_h(x_{l \rightarrow h}). \quad (5)$$

### 3.2. Network Learning

To learn the proposed network, we design image domain losses and shape domain losses that leverage the adversarial learning as well as various form of consistencies between the inputs and outputs to obviate the need for the groundtruth data of  $x_l$ .

**Image domain losses.** Image domain losses encourage the network to generate the four outputs  $\{x_{i \rightarrow j} \mid i \in \{l, h\}, j \in \{l, h\}\}$  as intended, i.e.,  $x_{i \rightarrow j}$  should match the content of  $x_i$  and look like a sample from  $X_j$ .

*Adversarial loss.* For the two outputs  $x_{l \rightarrow h}$  and  $x_{h \rightarrow l}$ , there are no groundtruth data available. Therefore, we apply adversarial learning to encourage that  $x_{l \rightarrow h}/x_{h \rightarrow l}$  looks like a sample from  $X_h/X_l$ :

$$\begin{aligned} \mathcal{L}_{adv}^l &= \mathbb{E}_{X_l}[\log D_l(x_l)] + \mathbb{E}_{X_l, X_h}[1 - \log D_l(x_{h \rightarrow l})], \\ \mathcal{L}_{adv}^h &= \mathbb{E}_{X_h}[\log D_h(x_h)] + \mathbb{E}_{X_l, X_h}[1 - \log D_h(x_{l \rightarrow h})], \\ \mathcal{L}_{adv} &= \mathcal{L}_{adv}^l + \mathcal{L}_{adv}^h, \end{aligned} \quad (6)$$

where  $D_l/D_h$  is a discriminator that decides if the input is a sample from  $X_l/X_h$  or a synthetic data.

*Artifact consistency loss.* The adversarial loss only encourages  $x_{l \rightarrow h}/x_{h \rightarrow l}$  to look like a sample from  $X_h/X_l$  but does not encourage their content to match  $x_l/x_h$ . To impose this content preciseness, we employ a artifact consistency loss [13]:

$$\mathcal{L}_{art} = \mathbb{E}_{X_l, X_h}[\|(x_l - x_{l \rightarrow h}) - (x_h - x_{h \rightarrow l})\|_1]. \quad (7)$$

The loss ensures that the same artifact is removed from  $x_l$  and added to  $x_{h \rightarrow l}$ . Meanwhile, minimizing the loss keeps the synthetic image  $x_{l \rightarrow h}/x_{h \rightarrow l}$  anatomically close to the original one  $x_l/x_h$ .

*Image reconstruction loss.* The two outputs  $x_{l \rightarrow l}$  and  $x_{h \rightarrow h}$  are encoded and decoded entirely using the latent codes of  $x_l$  and  $x_h$ , respectively, which essentially are autoencodings. Thus, we use L1 loss to regularize the pixel-wise distance between the inputs and the reconstructed images in each image domain,

$$\mathcal{L}_{rec} = \mathbb{E}_{X_l, X_h}[\|x_l - x_{l \rightarrow l}\|_1 + \|x_h - x_{h \rightarrow h}\|_1], \quad (8)$$

L1 loss is known to retain the sharpness compared with L2 loss [10].

*Self-reduction loss.* We also apply the cycle consistency mechanism [30, 8, 14] for  $\mathcal{C} : X_h \rightarrow X_l \rightarrow X_h$ . That is, the artifacts generated in  $x_{h \rightarrow l}$  can also be removable by our model by applying  $E_l \circ G_h$ , which recovers the input  $x_h$ :

$$\mathcal{L}_{self} = \mathbb{E}_{X_l, X_h}[\|G_h(E_l(x_{h \rightarrow l}), G_s(E_l(x_{h \rightarrow l}))) - x_h\|_1]. \quad (9)$$

**Shape domain losses.** Shape domain losses leverage the vertebra shapes  $y_h^{gt}$  from  $\mathcal{D}_h$  and discover the shape consistencies for the learning of the two segmentors  $S_l$  and  $S_h$ .

*Shape loss.* The segmentor  $S_h$  takes an image from  $X_h$  and outputs the corresponding vertebra shape prediction. We supervise the segmentation of  $x_h$  and  $x_{h \rightarrow h}$  with  $y_h^{gt}$  by Dice loss:

$$\begin{aligned} \mathcal{L}_x^s &= \mathbb{E}_{X_h} \left[ \left( 1 - \frac{2 \sum_k y_h(k) \odot y_h^{gt}(k)}{\sum_k (y_h(k) + y_h^{gt}(k))} \right) \right. \\ &\quad \left. + \left( 1 - \frac{2 \sum_k y_{h \rightarrow h}(k) \odot y_h^{gt}(k)}{\sum_k (y_{h \rightarrow h}(k) + y_h^{gt}(k))} \right) \right], \end{aligned} \quad (10)$$

where  $k$  denotes the pixel index. The Dice loss is first introduced by Milletari *et al.* [15], which alleviates the imbalance problem between foreground and background pixels and greatly improves the segmentation performance.

*Shape loss related to content code.*  $m_h$  is decoded from content code  $c_h$  by  $G_s$ . We compute Dice loss between prediction  $m_h$  and ground truth  $y_h^{gt}$ :

$$\mathcal{L}_c^s = \mathbb{E}_{X_h} \left[ 1 - \frac{2 \sum_k m_h(k) \odot y_h^{gt}(k)}{\sum_k (m_h(k) + y_h^{gt}(k))} \right]. \quad (11)$$

*Shape reconstruction loss.* As the anatomical information is supposed to be retained during reconstruction, the segmentation prediction  $y_l$  should be close to  $y_{l \rightarrow l}$ , and  $y_h$  should be close to  $y_{h \rightarrow h}$ . We use L1 loss to minimize the distance,

$$\mathcal{L}_{rec}^s = \mathbb{E}_{X_l, X_h}[\|y_l - y_{l \rightarrow l}\|_1 + \|y_h - y_{h \rightarrow h}\|_1]. \quad (12)$$



*Shape translation loss.* Similarly, we can apply L1 loss to minimize the distance between segmentation pairs  $(y_l, y_{l \rightarrow h})$  and  $(y_h, y_{h \rightarrow l})$  during translation,

$$\mathcal{L}_{trans}^s = \mathbb{E}_{X_l, X_h} [\|y_l - y_{l \rightarrow h}\|_1 + \|y_h - y_{h \rightarrow l}\|_1]. \quad (13)$$

**Total Loss.** The overall objective function is formulated as the weighed sum of all the above losses,

$$\begin{aligned} \mathcal{L}_{total} = & \lambda_{adv} \mathcal{L}_{adv} + \lambda_{rec} \mathcal{L}_{rec} + \lambda_{self} \mathcal{L}_{self} + \lambda_{art} \mathcal{L}_{art} \\ & + \lambda_c^s \mathcal{L}_c^s + \lambda_x^s \mathcal{L}_x^s + \lambda_{rec}^s \mathcal{L}_{rec}^s + \lambda_{trans}^s \mathcal{L}_{trans}^s, \end{aligned} \quad (14)$$

where  $\lambda_i$  is the weight for the loss of type  $i$ . In this paper, we empirically set the weights as  $\lambda_{adv} = 1, \lambda_{rec} = \lambda_{self} = \lambda_{art} = \lambda_c^s = \lambda_x^s = \lambda_{rec}^s = \lambda_{trans}^s = 5$ .

### 3.3. Implementation Details

Most of the network components of the proposed shape-aware artifact disentanglement network are developed based on the state-of-the-art works for image-to-image translation. For the encoders  $E_l, E_h$ , and  $E_a$ , we adopt the structure proposed by Huang *et al.* [8]. For the low-quality image decoder  $G_l$ , we employ a similar structure by Liao *et al.* [13] to fuse the artifact and content codes. In addition, we use the PatchGAN designed by Isola *et al.* [10] as our discriminators  $D_l$  and  $D_h$ . For the segmentors  $S_l$  and  $S_h$ , we simply use the U-Net architecture [19] with a depth of five. We use Sigmoid activation for the last convolutional layer to output the probability of a pixel belonging to vertebrae. We refer readers to the supplementary material for more detailed network structures.

To better retain the anatomical structure in the synthetic CT image, we adopt the idea of SPADE [16] and design a shape-aware normalization layer (see Figure 3a).  $G_s$  extracts the shape representation  $m_i, i \in \{l, h\}$  from content code  $c_i$ .  $m_i$  is then interpolated to match the spatial dimension of the input feature  $F_{in}$  and used as a soft semantic mask for SPADE. There are three Conv layers and a parameter-free batch-normalization (Norm) layer. The first Conv layer encodes interpolated  $m_i$  to a hidden space and then the other two Conv layers learn spatial related parameter  $\gamma$  and  $\beta$ . Meanwhile,  $F_{in}$  is only normalized without scale and shift with Norm. The normalized feature is denormalized with  $\gamma$  and  $\beta$  learned from  $m_i$ , resulting in the output  $F_{out}$ . The detailed structure of  $G_h$  is shown in Figure 3b. All the Norm layers in residual, upsampling and final blocks of  $G_h$  are replaced by the shape-aware normalization layer (i.e., SPADE). Our model benefits from the new structure in two aspects. First, the learned shape representation guides the synthesis, which prevents washing away the anatomical information. Second, the soft mask allow the gradients being back-propagated though disentanglement learning, which encourages the encoding of content code to be more accurate.

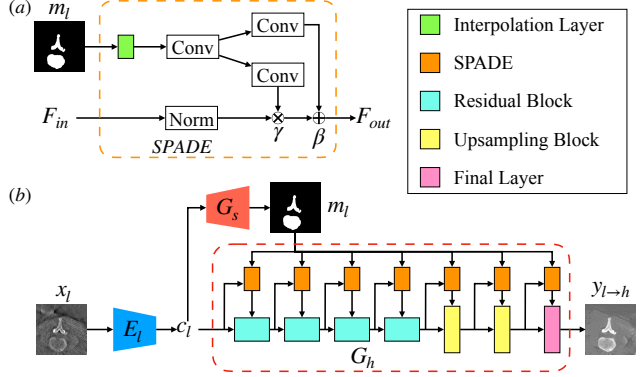


Figure 3. Detailed architecture. (a) Shape-aware normalization. (b) Decoder  $G_h$  with shape-aware normalization.

## 4. Experiment

### 4.1. Dataset

**CBCT data.** The CBCT data are collected by a Siemens Arcadis Orbic 3D system during spinal intervention. The dataset contains 26 scans. The size of CBCT volumes is  $256 \times 256 \times 256$ . The isotropic voxel size is 0.5 mm. Due to the severe cone-beam geometry distortion at the two ends of the sagittal axis, we only keep 196 slices in the middle for each volume. We use 21 volumes for training and 5 volumes for testing, resulting in 4116 slices in the training set and 980 slices in the testing set. To evaluate the segmentation performance, the vertebra masks for the testing set are manually labeled by an expert.

**CT data.** The Datasets 13<sup>2</sup> and 15 [26] of SpineWeb [6] are used as high-quality CT images. We include fifteen CT scans from Dataset 13 and twenty CT scans from Dataset 15. The scans from Datasets 13 and 15 cover the lumbar spine and the entire thoracic/lumbar spine, respectively. All the scans have corresponding segmentation masks for the vertebrae. The in-plane resolution is between 0.31 mm and 0.8 mm and the slice thickness is between 0.7 mm to 2 mm. We only include the CT slices with vertebrae in the experiment. To match the resolution and spatial dimension of CBCT image, all the CT slices are resampled to a spacing of 0.5 mm and randomly cropped to the size of  $256 \times 256$  with vertebrae present in the field of view. We withhold two scans from Dataset 13 and three scans from Dataset 15 for testing, resulting in 7,420 CT images for training and 1,937 for testing. Because there are more CT images than CBCT image, we randomly select 4,116 CT images for each epoch during training. For testing, we fix a randomly selected dataset of 980 CT images.

<sup>2</sup><http://lit.fe.uni-lj.si/xVertSeg/>

Dice/HD(mm)	$m_l$	$y_l$	$y_{l \rightarrow l}$	$y_{l \rightarrow h}$	$m_h$	$y_h$	$y_{h \rightarrow h}$	$y_{h \rightarrow l}$
M1	0.683/30.54	n.a./n.a.	n.a./n.a.	n.a./n.a.	0.938/9.74	n.a./n.a.	n.a./n.a.	n.a./n.a.
M2	0.737/30.57	n.a./n.a.	n.a./n.a.	n.a./n.a.	0.946/9.51	n.a./n.a.	n.a./n.a.	n.a./n.a.
M3	0.765/21.20	0.727/32.98	0.680/35.83	0.834/13.18	0.941/8.70	0.942/7.13	0.939/7.06	0.942/7.71
M4	0.815/22.59	0.861/12.04	0.861/12.06	0.818/19.33	<b>0.950/8.37</b>	<b>0.952/7.35</b>	<b>0.955/6.97</b>	<b>0.952/7.22</b>
M5	<b>0.847/16.16</b>	<b>0.879/10.54</b>	<b>0.879/10.56</b>	<b>0.879/10.33</b>	0.945/8.62	0.948/6.85	0.950/6.73	0.946/7.25

Table 1. Quantitatively evaluation segmentation performance for different models.

## 4.2. Training Details

We implement our model using the PyTorch framework [17] and train it for 48 epochs using the Adam optimizer with a learning rate of  $1 \times 10^{-4}$  and a batch size of 1. For data augmentation, the images and segmentation masks are randomly flipped horizontally during training.

## 4.3. Evaluation Methods

We evaluate the performance of vertebra segmentation using Dice score and Hausdorff Distance (HD) [4, 5, 1]. Dice score  $\in [0,1]$  measures the relative volumetric overlap between segmentations, and a perfect segmentation yields a Dice score of 1. HD is also known as maximum surface distance, which reflects the agreement between segmentation boundaries [22]. We obtain the segmentation mask from shape prediction by applying a threshold of 0.5.

## 4.4. Ablation Study

In this section, we investigate the effectiveness of different modules and objectives of the proposed architecture. Our backbone is ADN [13] using  $E_l$ ,  $E_h$ ,  $E_a$ ,  $G_l$ ,  $G_h$  and learning with  $\mathcal{L}_{adv}$ ,  $\mathcal{L}_{rec}$ ,  $\mathcal{L}_{self}$ ,  $\mathcal{L}_{art}$ . Note that  $G_h$  in ADN uses instance normalization. We use the following configurations for this ablation study:

- M1: ADN with shape decoder  $G_s$  and shape loss related to content code  $\mathcal{L}_c^s$ .
- M2: M1 with  $G_h$  using shape-aware normalization.
- M3: M2 with segmentors  $S_l$ ,  $S_h$  and shape loss  $\mathcal{L}_x^s$ .
- M4 : M3 with shape reconstruction loss  $\mathcal{L}_{rec}^s$ .
- M5 (full) : M4 with shape translation loss  $\mathcal{L}_{trans}^s$ .

Table 1 summarizes the quantitative evaluation results of vertebra segmentation performance of different models. Figure 4 shows the reconstructions and translations of a sample CBCT image  $x_l$  as well as the vertebra segmentation results and ground truth. In  $x_l$ , we can see a small metallic object above the vertebra, which is used for spinal surgery guidance. The metallic object introduces strong artifacts, such as bright and dark bands around the metal and streak artifacts nearly everywhere.

M1 can roughly disentangle artifacts and anatomical information. Figure 4 shows most of artifacts are suppressed in the synthetic CT image  $x_{l \rightarrow h}$  of M1, but streak artifacts are still visible in the lower part. The anatomical structure is not well retained in  $x_{l \rightarrow h}$  as the boundaries of vertebra are smoothed out. M1 learns to extract the shape of vertebra from content code with the supervision of target domain.  $m_h$  achieves a Dice of 0.938, but  $m_l$  only reaches a Dice of 0.683. The segmentation performance  $m_l$  is not satisfying.

**The effect of shape-aware normalization.** The proposed normalization layer improves the segmentation performance as well as the quality of synthetic image. From M1 to M2, the Dice of  $m_l$  is increased by 0.054, and  $m_l$  captures more bony structure. The translated image  $x_{l \rightarrow h}$  of M2 is sharper and with better contrast compared with M1. With the special structure,  $G_s$  is able to be punished in image translation and reconstruction process and the other encoders and decoders receive more guidance.

**The effect of shape loss.** M3 highly improves the segmentation performances for  $m_l$  and  $m_h$  with two additional segmentors. Among all the CBCT segmentations,  $y_{l \rightarrow h}$  achieves the best performance with a Dice of 0.834 and a HD of 13.14 mm. With the fully supervised  $S_h$ , M3 learns to predict accurate vertebra shape from translated CT image. The segmentation performance of  $m_l$  is also significantly improved. Compared with M2, its Dice is increased by 0.28 and the HD is decreased by 9.37 mm. But the performance of  $S_l$  on  $x_l$  or  $x_{l \rightarrow l}$  is relative low even when  $S_l$  is able to output precise segmentation  $y_{h \rightarrow l}$  for  $x_{h \rightarrow l}$  with a Dice of 0.939. As shown in Figure 4, there are lots of false positive and false negative errors in  $y_l$  and  $y_{l \rightarrow l}$ . It is because  $S_l$  is confused by the bright bands around the metal, which have the same intensity as bone, moreover, the streak artifacts distort the lower bone structure.

**The effect of shape reconstruction and translation constraints.** When the shape representation is retained during reconstruction for both domains, M4 achieves better segmentation performances for all the CT and CBCT images but not for  $x_{l \rightarrow h}$ , compared with M3. As shown in Figure 4,  $y_l$  and  $y_{l \rightarrow l}$  are hugely improved with  $\mathcal{L}_{rec}^s$ , but the segmentation of  $x_{l \rightarrow h}$  becomes too sensitive and false positive predictions show up. After adding  $\mathcal{L}_{trans}^s$ , all the segmentations of CBCT images in M5 are further improved.

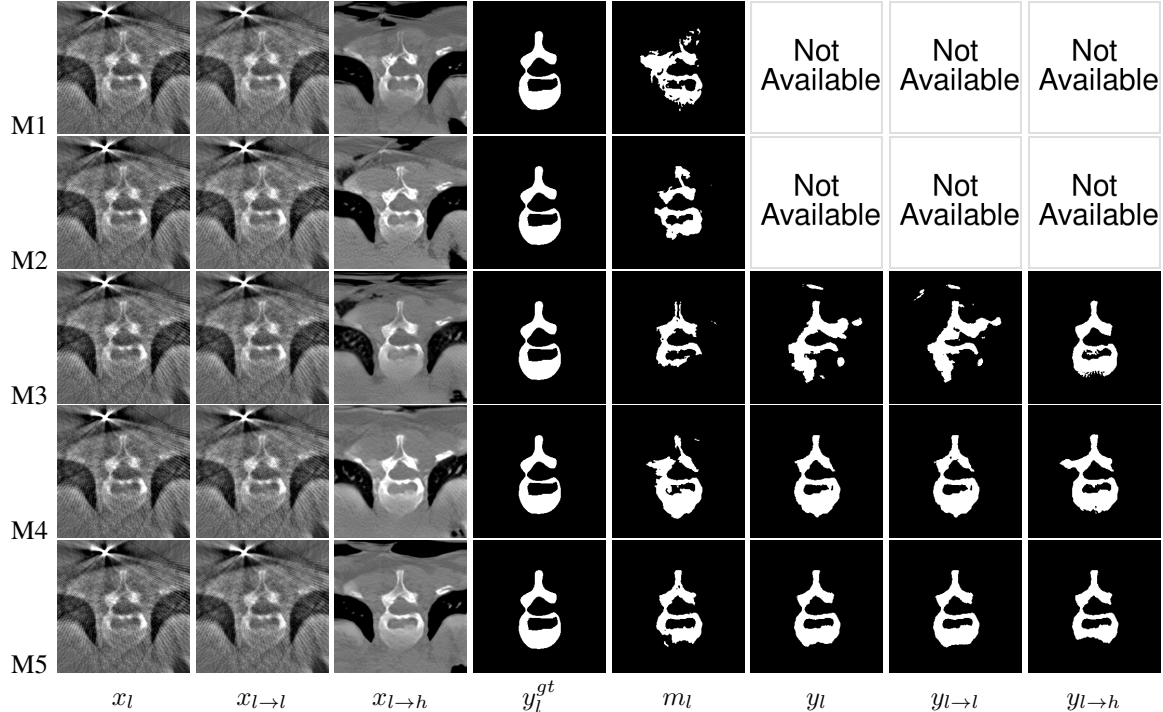


Figure 4. Qualitative comparison for image translation and segmentation of different variants of our model.

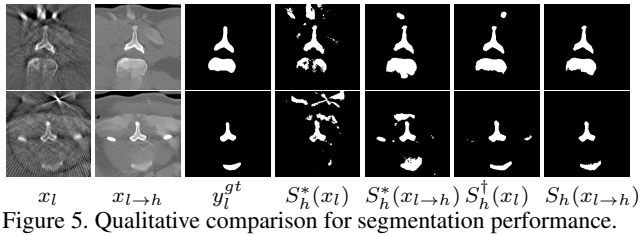


Figure 5. Qualitative comparison for segmentation performance.

From Figure 4, we can observe the false positive predictions of  $y_{l \to h}$  in M4 are suppressed and  $m_l$  becomes more realistic.  $y_{l \to h}$  in M5 yields the best segmentation performance for CBCT images with a Dice of 0.879 and a HD of 10.33 mm. For the synthetic CT image, M4 recovers the right rib bone which is smoothed out by M3. Overall, M5 generates  $x_{l \to h}$  with best image quality among all the models, which is with the best metal artifact reduction performance and bone contrast.

**The effect of explicit segmentors.** As shown in Figure 2, the segmentor  $S_i, i \in \{l, h\}$  can also be replaced by a combination of  $E_i$  and  $G_s$ . We train a model with such replacements and the same losses as M5, where  $y_i$  is replaced by  $m_i$ . The best segmentation performance on CBCT images is  $y_{l \to h}$  with a Dice of 0.850 and a HD of 15.00 mm, which is worse than M5. Large errors in  $y_{l \to h}$  as well as false bone structures in  $x_{l \to h}$  indicate the model can not capture the anatomical priors correctly when the attention map and segmentation are forced to be identical.

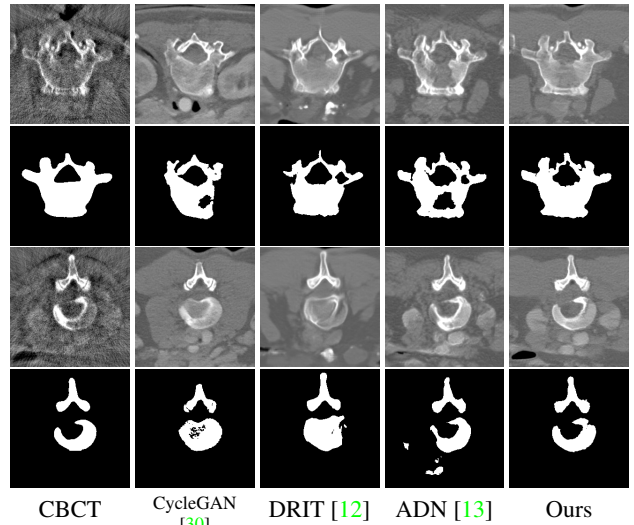


Figure 6. Qualitative comparison for synthesis quality.

Dice/HD(mm)	$x_h$	$x_l$	$x_{l \to h}$
$S_h^*$	<b>0.952</b> /8.91	0.734/42.17	0.825/20.80
$S_h^\dagger$	0.923/27.84	0.787/23.17	n.a./n.a.
$S_h$	0.950/ <b>6.85</b>	n.a./n.a.	<b>0.879/10.33</b>

Table 2. Quantitative evaluation for segmentation performance of joint learning and domain adaptation.

#### 4.5. Evaluation

Since image synthesis and segmentation benefit from each other in joint learning. We evaluate our model from three aspects. First, we prove the joint learning boosts the performance of segmentors for both domains. Second, we use a vertebra segmentor trained only in CT domain to compare the quality of synthetic CT images of our model and the state-of-the-art methods. Third, we compare the MAR performances qualitatively.

**Segmentation.** The conventional approach for unsupervised segmentation is through domain adaption or image synthesis. To segmented the translated CBCT image [24], we train another segmentor  $S_h^*$  with the same architecture as  $S_h$  based on paired CT images and masks for 50 epochs. Following [11], we fine tune  $S_h^*$  with an adversarial network to learn domain invariant features from multiple layers on CBCT images for another 50 epochs. The domain adapted model is referred as  $S_h^\dagger$ . The results are summarized in Table 2. Applying  $S_h^*$  directly on CBCT images serves as a lower-bound performance (Dice: 0.743) and the predictions are discrete.  $S_h^*$  benefits from image translation when applied on  $x_{l \rightarrow h}$  and the performance is acceptable (Dice: 0.825). With domain adaption,  $S_h^\dagger$  achieves a better performance on  $x_l$  (Dice: 0.787) but worse performance on  $x_h$  (Dice: 0.923). The segmentors with domain adaption and image translation output plausible predictions but the performance is affected by metal artifact and unrelated bones, as shown in Figure 5. The jointly learned  $S_h$  greatly improves the segmentation performance on  $x_{l \rightarrow h}$  (Dice: 0.879). Moreover, the segmentation performance in source domain can also be boosted as the HD of CT segmentation results is decreased by 2.06 mm.

**Modality translation.** We use the performance of  $S_h^*$  on synthetic CT images as an anatomy-invariant evaluator to compare the image synthesis performance of our model with the state-of-the-arts methods: CycleGAN [30], DRIT [12], ADN [13]. All the models are trained with our data using their officially released codes. As shown in Table 3, our model achieves the best performance with a much larger Dice compared with all the other methods. From Figure 6, we can observe our model performs significantly better than other methods in image translation. CycleGAN and DRIT tend to output plausible and realistic CT images

Dice/HD(mm)	Synthetic CT
CycleGAN [30]	0.727/26.01
DRIT [12]	0.718/ <b>20.21</b>
ADN [13]	0.764/21.86
Our Model	<b>0.825</b> /20.80

Table 3. Quantitative evaluation for synthesis quality.

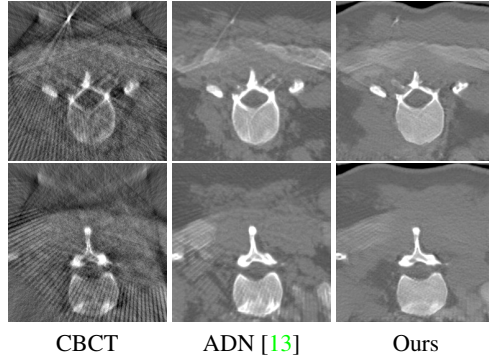


Figure 7. Qualitative comparison for MAR performance.

but are not able to preserve the anatomical information precisely. As shown in the segmentation results in Figure 6, the bony structures are distorted and scratched. With the help of  $\mathcal{L}_{art}$ , ADN can retain most of the anatomical information but not the bone pixels with high intensity. ADN may classify the high intensity bone pixels into metal artifact. With the anatomical knowledge from CT domain, our model learns to output high-quality synthetic CT images while keeping anatomy consistency.

**Metal artifact reduction.** Here we only present the MAR performance of ADN and our model since the distorted anatomical structure makes CycleGAN and DRIT less valuable. As shown in Figure 7, our model outperforms ADN. The shadow of streak artifacts and bright bands remain in the synthetic CT images of ADN, while our model can suppress all the artifacts and keep the bone edges sharp.

#### 5. Conclusions

We present a unified framework to jointly address three seemingly different tasks: unpaired modality translation, unsupervised segmentation and artifact reduction. In particular, we propose to jointly train encoders and decoders with segmentors and a shape-aware normalization layer to utilize the vertebra-shape knowledge across domains. Extensive experimental results demonstrate that the segmentation accuracy, image synthesis quality and MAR performance of our model are better than those obtained by the state-of-the-art methods and the conventional single-task unsupervised segmentation framework.

#### References

- [1] P. F. Christ, F. Ettliger, F. Grün, M. E. A. Elshaera, J. Lipkova, S. Schlecht, F. Ahmaddy, S. Tatavarty, M. Bickel, P. Bilic, et al. Automatic liver and tumor segmentation of ct and mri volumes using cascaded fully convolutional neural networks. *arXiv preprint arXiv:1702.05970*, 2017. 6
- [2] Q. Dou, C. Ouyang, C. Chen, H. Chen, and P.-A. Heng. Unsupervised cross-modality domain adaptation of convnets for biomedical image segmentations with adversarial loss. *arXiv preprint arXiv:1804.10916*, 2018. 3



- [3] V. Dumoulin, J. Shlens, and M. Kudlur. A learned representation for artistic style. *arXiv preprint arXiv:1610.07629*, 2016. 2
- [4] E. Gibson, F. Giganti, Y. Hu, E. Bonmati, S. Bandula, K. Gurusamy, B. Davidson, S. P. Pereira, M. J. Clarkson, and D. C. Barratt. Automatic multi-organ segmentation on abdominal ct with dense v-networks. *IEEE transactions on medical imaging*, 37(8):1822–1834, 2018. 6
- [5] E. Gibson, W. Li, C. Sudre, L. Fidon, D. I. Shaker, G. Wang, Z. Eaton-Rosen, R. Gray, T. Doel, Y. Hu, et al. Niftynet: a deep-learning platform for medical imaging. *Computer methods and programs in biomedicine*, 158:113–122, 2018. 6
- [6] B. Glocker, D. Zikic, E. Konukoglu, D. R. Haynor, and A. Criminisi. Vertebrae localization in pathological spine ct via dense classification from sparse annotations. In *International Conference on Medical Image Computing and Computer-Assisted Intervention*, pages 262–270. Springer, 2013. 5
- [7] X. Huang and S. Belongie. Arbitrary style transfer in real-time with adaptive instance normalization. In *Proceedings of the IEEE International Conference on Computer Vision*, pages 1501–1510, 2017. 2
- [8] X. Huang, M.-Y. Liu, S. Belongie, and J. Kautz. Multimodal unsupervised image-to-image translation. In *Proceedings of the European Conference on Computer Vision (ECCV)*, pages 172–189, 2018. 2, 4, 5
- [9] S. Ioffe and C. Szegedy. Batch normalization: Accelerating deep network training by reducing internal covariate shift. *arXiv preprint arXiv:1502.03167*, 2015. 2
- [10] P. Isola, J.-Y. Zhu, T. Zhou, and A. A. Efros. Image-to-image translation with conditional adversarial networks. In *Proceedings of the IEEE conference on computer vision and pattern recognition*, pages 1125–1134, 2017. 2, 4, 5
- [11] K. Kamnitsas, C. Baumgartner, C. Ledig, V. Newcombe, J. Simpson, A. Kane, D. Menon, A. Nori, A. Criminisi, D. Rueckert, et al. Unsupervised domain adaptation in brain lesion segmentation with adversarial networks. In *International conference on information processing in medical imaging*, pages 597–609. Springer, 2017. 3, 8
- [12] H.-Y. Lee, H.-Y. Tseng, J.-B. Huang, M. Singh, and M.-H. Yang. Diverse image-to-image translation via disentangled representations. In *Proceedings of the European Conference on Computer Vision (ECCV)*, pages 35–51, 2018. 2, 7, 8
- [13] H. Liao, W.-A. Lin, S. K. Zhou, and J. Luo. Artifact disentanglement network for unsupervised metal artifact reduction. *arXiv preprint arXiv:1906.01806*, 2019. 2, 3, 4, 5, 6, 7, 8
- [14] M.-Y. Liu, T. Breuel, and J. Kautz. Unsupervised image-to-image translation networks. In *Advances in neural information processing systems*, pages 700–708, 2017. 2, 4
- [15] F. Milletari, N. Navab, and S.-A. Ahmadi. V-net: Fully convolutional neural networks for volumetric medical image segmentation. In *2016 Fourth International Conference on 3D Vision (3DV)*, pages 565–571. IEEE, 2016. 4
- [16] T. Park, M.-Y. Liu, T.-C. Wang, and J.-Y. Zhu. Semantic image synthesis with spatially-adaptive normalization. In *Proceedings of the IEEE Conference on Computer Vision and Pattern Recognition*, pages 2337–2346, 2019. 2, 5
- [17] A. Paszke, S. Gross, S. Chintala, G. Chanan, E. Yang, Z. DeVito, Z. Lin, A. Desmaison, L. Antiga, and A. Lerer. Automatic differentiation in pytorch. 2017. 6
- [18] R. Pauwels, H. Stamatakis, H. Bosmans, R. Bogaerts, R. Jacobs, K. Horner, K. Tsiklakis, and S. P. Consortium. Quantification of metal artifacts on cone beam computed tomography images. *Clinical oral implants research*, 24:94–99, 2013. 1
- [19] O. Ronneberger, P. Fischer, and T. Brox. U-net: Convolutional networks for biomedical image segmentation. In *International Conference on Medical image computing and computer-assisted intervention*, pages 234–241. Springer, 2015. 5
- [20] S. Schafer, S. Nithianathan, D. Mirota, A. Uneri, J. W. Stayman, W. Zbijewski, C. Schmidgunst, G. Kleinszig, A. J. Khanna, and J. Siewerdsen. Mobile c-arm cone-beam ct for guidance of spine surgery: Image quality, radiation dose, and integration with interventional guidance. *Medical physics*, 38(8):4563–4574, 2011. 1
- [21] J. H. Siewerdsen. Cone-beam ct with a flat-panel detector: From image science to image-guided surgery. *Nuclear Instruments and Methods in Physics Research Section A: Accelerators, Spectrometers, Detectors and Associated Equipment*, 648:S241–S250, 2011. 1
- [22] A. A. Taha and A. Hanbury. An efficient algorithm for calculating the exact hausdorff distance. *IEEE transactions on pattern analysis and machine intelligence*, 37(11):2153–2163, 2015. 6
- [23] D. Ulyanov, A. Vedaldi, and V. Lempitsky. Improved texture networks: Maximizing quality and diversity in feed-forward stylization and texture synthesis. In *Proceedings of the IEEE Conference on Computer Vision and Pattern Recognition*, pages 6924–6932, 2017. 2
- [24] J. Yang, N. C. Dvornek, F. Zhang, J. Chapiro, M. Lin, and J. S. Duncan. Unsupervised domain adaptation via disentangled representations: Application to cross-modality liver segmentation. In *International Conference on Medical Image Computing and Computer-Assisted Intervention*, pages 255–263. Springer, 2019. 3, 8
- [25] Q. Yang, P. Yan, Y. Zhang, H. Yu, Y. Shi, X. Mou, M. K. Kalra, Y. Zhang, L. Sun, and G. Wang. Low-dose ct image denoising using a generative adversarial network with wasserstein distance and perceptual loss. *IEEE transactions on medical imaging*, 37(6):1348–1357, 2018. 1
- [26] J. Yao, J. E. Burns, D. Forsberg, A. Seitel, A. Rasouljan, P. Abolmaesumi, K. Hammernik, M. Urschler, B. Ibragimov, R. Korez, et al. A multi-center milestone study of clinical vertebral ct segmentation. *Computerized Medical Imaging and Graphics*, 49:16–28, 2016. 5
- [27] Y. Zhang and H. Yu. Convolutional neural network based metal artifact reduction in x-ray computed tomography. *IEEE Trans. Med. Imaging*, 37(6):1370–1381, 2018. 1
- [28] Y. Zhang, L. Zhang, X. R. Zhu, A. K. Lee, M. Chambers, and L. Dong. Reducing metal artifacts in cone-beam ct images by preprocessing projection data. *International Journal*

*of Radiation Oncology\* Biology\* Physics*, 67(3):924–932, 2007. [1](#)

- [29] Z. Zhang, L. Yang, and Y. Zheng. Translating and segmenting multimodal medical volumes with cycle-and shape-consistency generative adversarial network. In *Proceedings of the IEEE Conference on Computer Vision and Pattern Recognition*, pages 9242–9251, 2018. [2](#)
- [30] J.-Y. Zhu, T. Park, P. Isola, and A. A. Efros. Unpaired image-to-image translation using cycle-consistent adversarial networks. In *Proceedings of the IEEE international conference on computer vision*, pages 2223–2232, 2017. [2](#), [4](#), [7](#), [8](#)